

# Two-step nucleation of the Earth's inner core

Yang Sun,<sup>1,\*</sup> Feng Zhang,<sup>2</sup> Mikhail I. Mendelev,<sup>2,†</sup> Renata M. Wentzcovitch,<sup>1,3,4</sup> and Kai-Ming Ho<sup>5</sup>

<sup>1</sup>*Department of Applied Physics and Applied Mathematics,  
Columbia University, New York, NY 10027, USA*

<sup>2</sup>*Ames Laboratory, US Department of Energy, Ames, Iowa 50011, USA*

<sup>3</sup>*Department of Earth and Environmental Sciences,  
Columbia University, New York, NY 10027, USA*

<sup>4</sup>*Lamont-Doherty Earth Observatory, Columbia University, Palisades, NY 10964, USA*

<sup>5</sup>*Department of Physics, Iowa State University, Ames, Iowa 50011, USA*

(Dated: May 16, 2021)

It has long been assumed the Earth's solid inner core started to grow when molten iron cooled to its melting point. However, the nucleation mechanism, which is a necessary step of crystallization, has not been well understood. Recent studies found it requires an unrealistic degree of undercooling to nucleate the stable hexagonal close-packed (hcp) phase of iron, which can never be reached under the actual Earth's core conditions. This contradiction leads to the inner core nucleation paradox [1]. Here, using a persistent-embryo method and molecular dynamics simulations, we demonstrate that the metastable body-centered cubic (bcc) phase of iron has a much higher nucleation rate than the hcp phase under inner-core conditions. Thus, the bcc nucleation is likely to be the first step of inner core formation instead of direct nucleation of the hcp phase. This mechanism reduces the required undercooling of iron nucleation, which provides a key factor to solve the inner-core nucleation paradox. The two-step nucleation scenario of the inner core also opens a new avenue for understanding the structure and anisotropy of the present inner core.

The core plays a central role in the Earth's interior. The present core contains two major parts, a solid inner core and a liquid outer core. Iron dominates both parts with a small amount of light elements [2]. The solid core is generally believed to be hcp iron, while the possible existence of bcc iron has also been suggested [3–6]. The growth of the solid inner core is believed to be the major driving force of the present geodynamo, providing the main power source for convection in the liquid core [7, 8]. Despite its importance, the initial formation of the solid core, which directly relates to its thermal evolution and Earth's history, is far from being completely understood [9–13]. Most of Earth's thermal history models assume that the inner core started to crystallize when molten iron cooled right below its melting temperature at the Earth's center [8]. However, in practice, nucleation does not happen at the melting point but requires some undercooling because of the formation of a solid-liquid interface (SLI) that accompanies it. While the bulk solid phase is thermodynamically favored, the SLI costs energy. These two factors lead to a nucleation barrier  $\Delta G$ , which is described in classical nucleation theory (CNT) [14] as

$$\Delta G = N\Delta\mu + A\gamma, \quad (1)$$

where  $N$  is the nucleus size,  $\Delta\mu$  ( $< 0$ ) is the free energy difference between the bulk solid and liquid,  $\gamma$  ( $> 0$ ) is the SLI free energy, and  $A$  is the SLI area. The liquid must be cooled sufficiently below the melting temperature to overcome the free energy barrier during thermal fluctuations. After considering this mechanism, it was

found that a very large undercooling of  $\sim 1000$  K is required for the nucleation of hcp iron in the Earth's core [1]. However, considering the slow cooling rate of  $\sim 100$  K/Gyr throughout the core history [15], it is impossible to reach such a large degree of undercooling inside the Earth within the inner core's age. This “inner core nucleation paradox”, recently described by Huguet *et al.* [1], strongly challenges the current understanding of the inner core formation process. While Huguet *et al.*'s argument relies on a few estimations of thermodynamic quantities, Davies *et al.* also confirmed the paradox with atomic-scale simulations [16]. Even considering the effect of light elements on the nucleation process, it still requires 675 K undercooling to nucleate hcp iron, nearly impossible to reach in the Earth core [16].

Instead of the scenario described above, where the melt in the Earth's core crystallized directly into the hcp phase, we can consider a complex process where nucleation is facilitated by forming a metastable phase with a high nucleation rate [17, 18]. For example, it has been observed that the bcc phase can nucleate before face-centered cubic (fcc) or hcp phases in a few alloys where the fcc/hcp phase is the most stable one [19–23]. Could the bcc phase also facilitate hcp iron nucleation and relate to the inner core nucleation paradox? Making a quantitative prediction on such complex nucleation processes is a challenging problem. Despite the unreachable core conditions, nucleation involves microscopic length scales that are extremely hard to probe in real-time, even with state-of-the-art measurement [24]. Hence, it requires computer simulations, particularly large-scale molecular

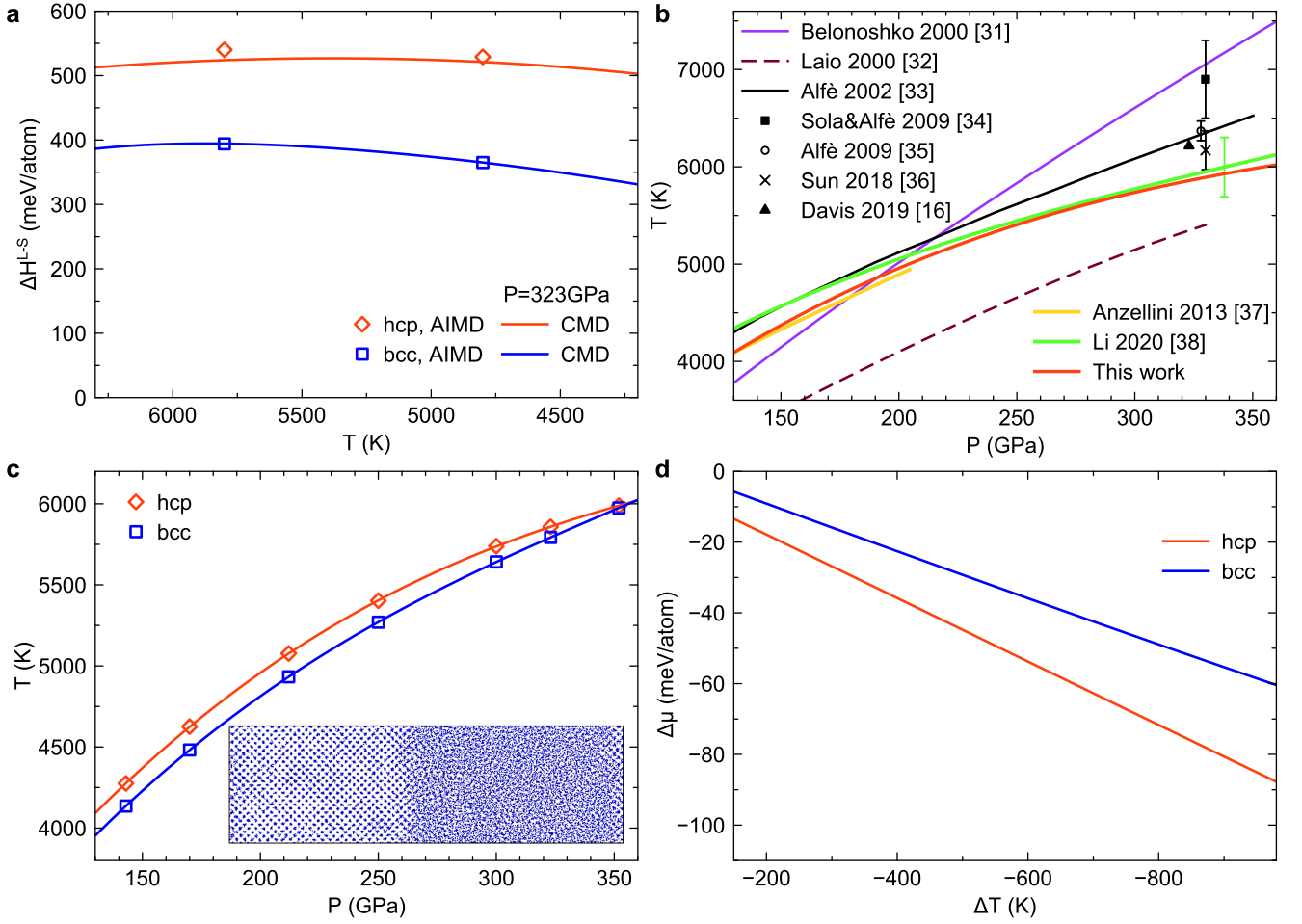


FIG. 1. **Melting curves and thermodynamic properties of hcp and bcc iron.** a, The latent heats of hcp and bcc iron at 323 GPa from AIMD and CMD with the developed semi-empirical potential. b, Comparison between the current melting curve of hcp iron and several others obtained by previous simulations and experiments [16, 31–38]. c, Melting curves of hcp and bcc iron from CMD with the developed semi-empirical potential. The inset shows a projected snapshot of the bcc solid-liquid coexistence simulation. d, Change in bulk free energy upon solidification (nucleation driving force) at 323 GPa.

dynamics (MD), to reproduce the temporal evolution of the liquid into the crystal [25]. Unfortunately, nucleation under Earth’s core conditions is a rare event that occurs on the geological time scale, far beyond the reach of any conventional MD simulations. Besides, any large-scale MD simulation requires a semi-empirical potential to describe atomic interactions, and the outcome may heavily depend on the quality of the potential [26, 27]. In this work, we assess the inner-core nucleation process with the account of competition between bcc and hcp phases during the nucleation process using the persistent-embryo method (PEM) to overcome the significant time limitation in conventional MD simulation of nucleation [28].

The nucleation rates of hcp iron estimated in previous work [1] were based on the values of the driving force and SLI free energy obtained in [29] with the semi-empirical potential developed in [30]. However, this potential was

developed to simulate iron at ambient conditions such that no high-pressure data were used in the potential development [30]. In the present study, we developed a potential explicitly considering its application at Earth’s core conditions. The details of the potential development are in Supplementary Information. One of the vital target properties in the potential development is the latent heat  $\Delta H^{L-S}$ , because along with the melting temperature it defines the driving force for the solidification. Figure 1a shows excellent agreement between the latent heat calculated using the developed potential and *ab initio* MD (AIMD) for both the hcp and bcc phases. Besides, elastic properties and liquid structure predicted with the developed potential also agree well with those calculated with AIMD (see Supplementary Information), making this potential suitable for simulations of the iron crystallization process under inner-core conditions.

In Fig. 1b, we compare the current melting curve of the hcp phase with previous measurements and simulation results [16, 31–38]. This is especially important because melting curves from previous classical MD (CMD) simulations deviate considerably from each other [31, 32], which points out the importance of employing a thoroughly developed semi-empirical potential. The melting temperatures in the present study were determined at several pressures using the solid-liquid coexistence approach [39]. The current melting curve agrees well with the experimental curve obtained using fast x-ray diffraction in the laser-heated diamond anvil cell in the pressure range between 130 GPa and 200 GPa [37]. It also reasonably agrees with the recent estimation of melting boundary from shock compression measurements in the higher pressure range from 250 GPa to 360 GPa [38]. Compared to previous simulations, our current melting curve provides the closest agreement to the recent high-pressure experiments for the hcp phases.

The melting curves of hcp and bcc phases are compared in Figure 1c. The hcp phase has higher melting temperatures in the pressure range from 130 GPa to 330 GPa. Thus, the hcp phase is thermodynamically stable, while the bcc phase is metastable in the range from the core-mantle boundary to the inner core boundary. Interestingly, the melting points of hcp and bcc phases are predicted to be very close after 330 GPa and crossover at 360 GPa. As these pressures range from the core's center to the inner core boundary, this result suggests the inner core could have more than one layer with predominant hcp and bcc phases.

In the present study, we chose to conduct simulations of nucleation at 323 GPa, the pressure at the inner core boundary. We used the Gibbs-Helmholtz equation and MD simulation to calculate the free energy difference  $\Delta\mu$  between the bulk solid and liquid as described in [40]. Figure 1d shows  $\Delta\mu$  as a function of undercooling with respect to the hcp melting temperature,  $\Delta T = T - T_m^{\text{hcp}}$ , for both the hcp and bcc phases. The absolute value of  $\Delta\mu$  for the hcp phase is always larger than that for the bcc phase.

According to the CNT [14], the nucleation barrier  $\Delta G^*$  is the key quantity to determine the nucleation rate. It can be computed [28] as

$$\Delta G^* = \frac{1}{2} |\Delta\mu| N^*, \quad (2)$$

where  $N^*$  is the critical nucleus size. To obtain  $N^*$ , we employ the PEM [28], which invokes the central CNT concept that homogeneous nucleation happens via the formation of a critical nucleus in the undercooled liquid. Figure 2a shows a typical result of the PEM-MD simulation. The plateau on the MD trajectory indicates the appearance of the critical nucleus (see technical details in Methods). The critical nucleus sizes of both the hcp and bcc phases at several moderate undercooling tem-

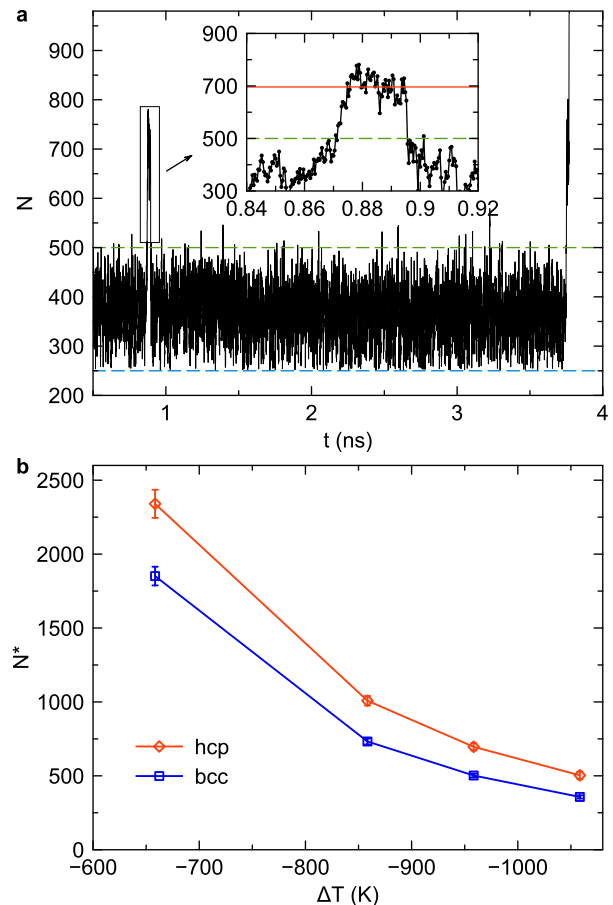


FIG. 2. **PEM-MD simulation and critical nucleus size.**

a, The nucleus size versus time of a PEM-MD trajectory at  $\Delta T = -958$  K (i.e.,  $T = 4900$  K). The blue dashed line shows the size of persistent embryo,  $N_0$ , and the green dashed line indicates the threshold for aping removal,  $N_{sc}$  (see Method). The inset enlarges the plateaus at the critical size. The red line indicates the plateaus to determine the critical nucleus size,  $N^*$ . b, The critical nucleus size as a function of undercooling temperature for hcp and bcc phases.

peratures are shown in Fig. 2b. The hcp phase shows a systematically larger critical nucleus size than the bcc phase. Figure 3a shows the free energy barriers  $\Delta G^*$  of both bcc and hcp phases computed using Eq. (2). The hcp phase has a larger nucleation barrier than the bcc phase at all undercooling temperatures considered here, although the hcp phase has a larger bulk driving force  $\Delta\mu$  in Fig. 1d. To explain this, we compare the SLI free energies of these phases obtained from the PEM simulation. Figure 3b shows that this quantity is much larger for the hcp phase. Because the  $\Delta G^*$  scales with  $\gamma^3$ , the difference in  $\gamma$  can significantly change the ratio of the nucleation barriers. The temperature dependences of the  $\gamma$  obtained for both hcp and bcc phases are almost linear as shown in Fig. 3b, which is similar to the ones found for Ni and Al in [41]. Therefore, the SLI free energy can

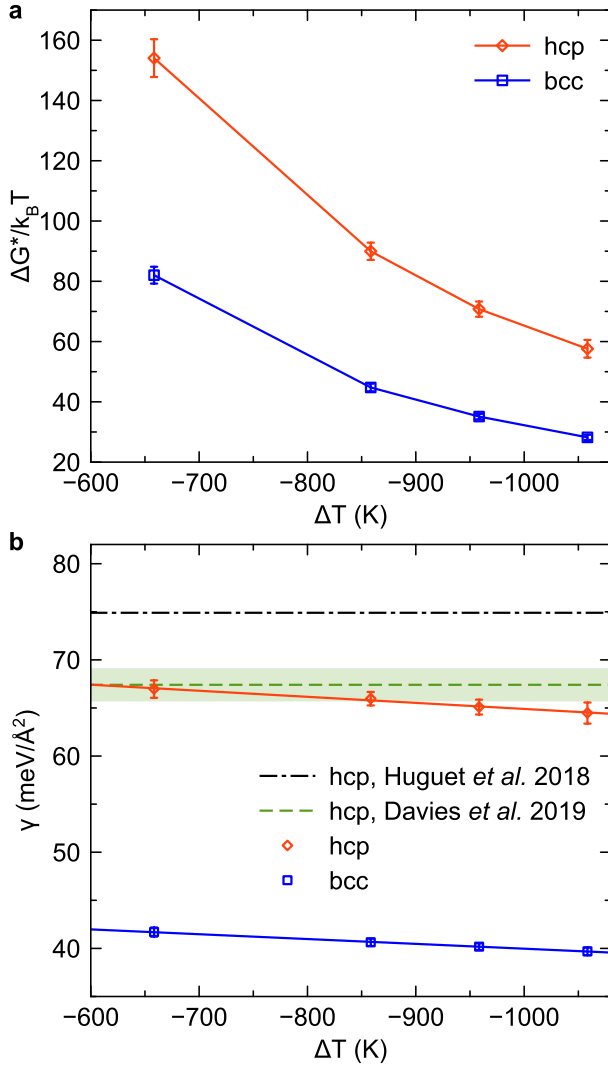


FIG. 3. **Temperature dependence of the free energy barrier and SLI free energy.** a, Free energy barrier  $\Delta G^*$  as a function of undercooling temperature for hcp and bcc at 323 GPa. b, SLI free energy of hcp and bcc phases at 323 GPa. The dashed dot line is from Ref.[1]. The dashed line with the confidence interval (green band) is from Ref.[16].

be linearly extrapolated to smaller undercooling (higher temperatures), where the critical nucleus size is too large to be simulated directly. In Fig. 3b we further compare the  $\gamma$  of hcp with previous data. Davies *et al.* computed the  $\gamma$  based on a different semi-empirical potential and the seeding technique [16]. While the temperature dependence was not considered in that work, the value of  $\gamma$  is very similar to our data. In contrast, the value of the  $\gamma$  determined in Ref.[29] highly deviates from our data and Ref. [16]. This can be attributed to the fact that the empirical potential used in Ref.[29] was not designed to simulate iron under the Earth's core conditions.

The nucleation rate,  $J$ , can be calculated as  $J = \kappa \exp(-\Delta G^*/k_B T)$ , where  $k_B$  is the Boltzmann constant,

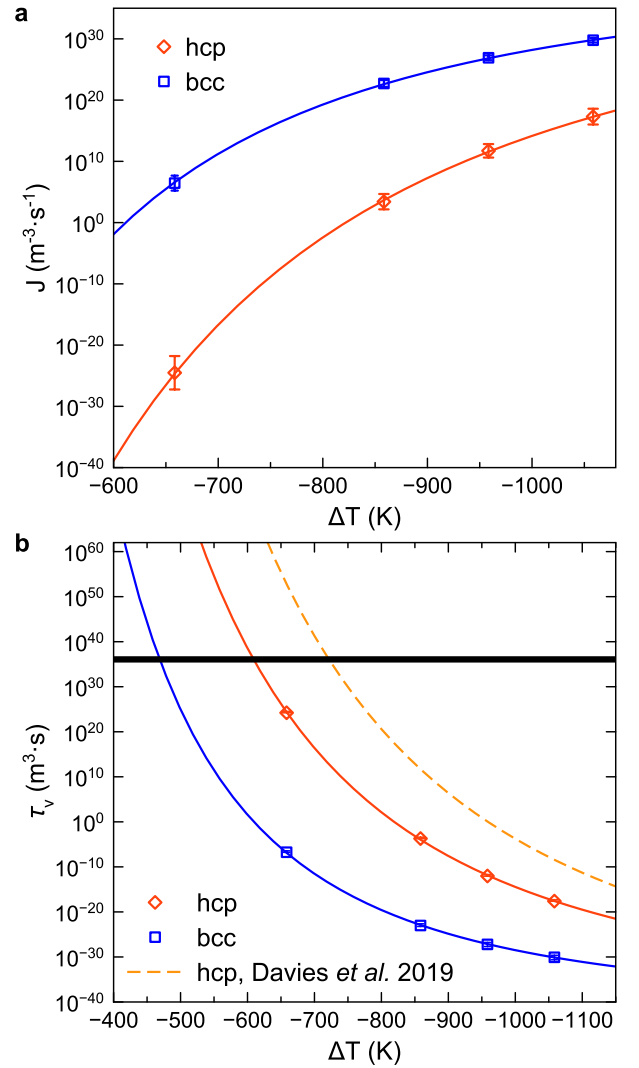


FIG. 4. **Nucleation rate and waiting time at 323 GPa.** a, Nucleation rate as a function of undercooling for the hcp and bcc phases. b, Waiting time as a function of undercooling. The dashed line is from Ref. [16]. The thick black line indicates the range of nucleation waiting time  $\tau_v$  in the Earth's core.

and  $\kappa$  is a kinetic prefactor. As demonstrated by Auer and Frenkel [42], the kinetic prefactor can be determined from MD simulations based on the fluctuations of the nucleus size around the critical value (see Supplementary Information). Thus we obtained all essential parameters to compare the bcc and hcp nucleation rates with PEM and MD. Figure 4a shows that the bcc phase has a much higher nucleation rate than the hcp phase in a broad undercooling regime. For example, at an undercooling of 660 K, the nucleation rate of the bcc phase is *31 orders of magnitudes* higher than that of the hcp phase. With such a vast difference, the bcc phase should always nucleate much quicker than the hcp phase under the Earth's core conditions.

Using the obtained nucleation rate, we are now able to estimate the nucleation waiting time. Because the critical nucleus only has half chance to grow at the top of the nucleation barrier, the waiting time in a fixed volume can be expressed as  $\tau_v = \frac{1}{2J}$  [16]. As shown in Fig. 4b, the present waiting time of hcp is smaller than the previous estimation by Davies *et al.* [16]. This is mainly because the semi-empirical potential used in [16] shows a different melting point and bulk free energy difference than the present values (see Supplementary Information). The reachable  $\tau_v$  in the Earth's core can be estimated as follows. The nucleation incubation time is approximated as one billion years, probably the upper limit of plausible inner core age [16]. The volumes of the inner core and the entire core are  $7.6 \times 10^{18} \text{ m}^3$  to  $1.8 \times 10^{20} \text{ m}^3$ . Therefore,  $\tau_v$  of the Earth's core should be in the range between  $2 \times 10^{35} \text{ m}^3 \cdot \text{s}$  to  $6 \times 10^{36} \text{ m}^3 \cdot \text{s}$ . By plotting these values and inspecting its intersection with hcp and bcc data in Fig. 4b, we obtain that the required undercooling is 470 K for bcc nucleation and 610 K for hcp nucleation. Therefore, the bcc phase significantly reduces the required undercooling of inner core nucleation by 140 K, which corresponds to 1.4 billion years of cooling based on a cooling rate of 100 K/Gyr [9].

Thus, we have shown the bcc nucleation is likely to be the first step of iron crystallization under the core conditions instead of directly nucleating the hcp phase. This reduces the required undercooling of inner core nucleation, which can be a key to solving the paradox. While the necessary undercooling of the bcc phase (470 K) is still more significant than the inner core's maxima undercooling of  $\sim 200 \text{ K}$  [1], a few factors remain to be accounted for. First, the core contains  $\sim 10 \text{ wt.}\%$  light elements. Davies *et al.* [16] have shown that oxygen can reduce the required undercooling by  $\sim 55 \text{ K}$  for the hcp phase. In bcc nucleation, the light elements should cause a similar, if not larger, reduction of the required undercooling. Because it has been demonstrated that the light elements can stabilize the bcc phase [5, 43–47], it will further increase the nucleation driving force. Moreover, the stresses associated with pressure variations can also reduce the undercooling by  $\sim 100 \text{ K}$  [16]. Considering these effects, it should be possible to solve the nucleation paradox with future development of semi-empirical or machine-learning potentials for iron and light elements and more sophisticated PEM nucleation simulations of a multi-component melt.

The two-step nucleation with the intermediate bcc phase can impact the present inner core structure. While the metastable bcc phase should eventually transform into the stable hcp phase at 323 GPa, the melting curves in Fig. 1c suggest the bcc phase could be stabilized over the hcp phase with the increasing pressure when approaching the core center. The initially formed bcc phase in this region may remain at the core center nowadays. This coincides with hypotheses of a different inner-

most core structure proposed to explain the anomalous anisotropy of the inner core [48–50]. Therefore, the two-step nucleation scenario of the inner-core formation opens a new path to understand the Earth's deepest interior.

## METHODS

**Ab initio molecular dynamics simulations** *Ab initio* molecular dynamics (AIMD) simulations were performed to obtain the input data for the semi-empirical potential development. The Vienna *Ab initio* Simulation Package (VASP) [51] was employed for the density-functional theory (DFT) calculations. The projected augmented-wave (PAW) method was used to describe the electron-ion interaction, and the generalized gradient approximation (GGA) in the Perdew-Burke-Ernzerhof (PBE) form was employed for the exchange-correlation energy functional. The electronic entropy at high temperature was described by the Mermin functional [52, 53]. The  $\Gamma$  point was used to sample the Brillouin zone. The AIMD simulations were performed for the constant number of atoms, volume and temperature (NVT) ensemble. The Nosé-Hoover [54] thermostat was employed to control the temperature. A time step of  $2.0 \text{ fs}$  was used to integrate Newton's equations of motion. Supercells with 288, 250, and 256 atoms were used to simulate hcp, bcc, and liquid models, respectively. To fit the potential for a large P-T range, three P-T conditions near the melting curves were investigated: 140 GPa at 4000 K, 250 GPa at 5500 K and 350 GPa at 6000 K. No phase transitions were observed during the simulation of either hcp, bcc or liquid model under these conditions during the AIMD simulations. To save time on the initial model equilibration, the AIMD simulations were run in an iterative manner with the potential development such that the available semi-empirical potential equilibrated the initial AIMD configurations. We monitored the energy and pressure as a function of time to determine when the models were equilibrated enough to start collecting data. These collections of data took place in the last 10 ps of each AIMD run.

**Classical Nucleation Theory formulas** Based on the CNT [14], the competition between the bulk and interface factors leads to the nucleation barrier. From Eq. (1), one can derive the nucleation barrier as

$$\Delta G^* = \frac{4s^3\gamma^3}{27\Delta\mu^2\rho_c^2}, \quad (3)$$

where  $\rho_c$  is the crystal density and  $s$  is a shape factor so that the interface area in Eq. (1) can be written as  $A = s(\frac{N}{\rho_c})^{2/3}$ . This equation can be simplified to Eq. (2) by replacing it with the critical nucleus size  $N^*$

$$N^* = \frac{8s^3\gamma^3}{27|\Delta\mu|^3\rho_c^3}, \quad (4)$$

From Eq. (4), one can derive the SLI free energy as

$$\gamma = \frac{3}{2s} |\Delta\mu| \rho_c^{\frac{2}{3}} N^{*\frac{1}{3}}. \quad (5)$$

The quantities to determine  $\gamma$  can all be obtained from MD simulations.

**Persistent-embryo method** The PEM [28] is employed to measure the critical nucleus size  $N^*$  with the classical MD simulations. It utilizes the main CNT concept that homogeneous nucleation happens via the formation of the critical nucleus in the undercooled liquid. During the simulation, a small crystal embryo containing  $N_0$  atoms (should be much smaller than the critical nucleus) is constrained by spring forces to prevent melting [28]. These forces are only applied to the original  $N_0$  embryo atoms. The spring constant of the harmonic potential decreases with increasing nucleus size as  $k(N) = k_0 \frac{N_{sc}-N}{N_{sc}}$  if  $N < N_{sc}$  and  $k(N) = 0$  otherwise. Here  $N_{sc}$  is a subcritical threshold. No spring forces are applied if  $N > N_{sc}$ . This strategy ensures that the system is unbiased at the critical point such that a reliable critical nucleus can be obtained. If the nucleus melts below  $N_{sc}$ , the harmonic potential is gradually enforced, preventing the complete melting of the embryo. When the nucleus reaches the critical size, it has an equal chance to melt or to further grow, causing fluctuations around  $N^*$ . As a result, the  $N(t)$  curve tends to display a plateau during the critical fluctuations, giving a unique signal to detect the appearance of the critical nucleus, as shown in Fig. 2a. The critical nucleus size is directly measured by averaging the nucleus size at the plateau [28]. We repeated the PEM-MD simulation to collect at least four plateaus to obtain sufficient statistics and the confidence interval of the critical nucleus size  $N^*$ .

The classical MD simulations of PEM were performed with the GPU (graphic processing unit)-accelerated LAMMPS (Large-scale Atomic/Molecular Massively Parallel Simulator) code [55–57]. The interatomic interaction was modeled using the semi-empirical potential developed in this work based on the embedded atom method (EAM) [58]. During the MD simulation, the constant number of atoms, pressure, and temperature (NPT) ensemble was applied with Nosé-Hoover thermostat and barostat. The damping time in the Nosé-Hoover thermostat was set as  $\tau = 0.1$  ps which is frequent enough for the heat dissipation during the crystallization [41]. The time step of the simulation was 1.0 fs. In some cases where the nucleation was very fast, the time step was 0.8 fs. The simulation cell contained 31,250 atoms which are at least 15 times larger than the critical nucleus size.

**Supplementary Information** The supplementary information contains details of semi-empirical potential development in Note S1, the calculation of the kinetic prefactor in Note S2, the effect of input parameters on the hcp waiting time in Note S3, and classification of hcp, bcc, and liquid with order parameters in Note S4.

## ACKNOWLEDGMENTS

This work was supported primarily by National Science Foundation awards EAR-1918134 and EAR-1918126. We acknowledge the computer resources from the Extreme Science and Engineering Discovery Environment (XSEDE), which is supported by National Science Foundation grant number ACI-1548562. R.M.W. and Y.S. also acknowledge partial support from the U.S. Department of Energy Grant DE-SC0019759. F.Z. acknowledges the support from U.S. Department of Energy, Basic Energy Sciences, Materials Science and Engineering Division, under Contract No. DEAC02-07CH11358.

**Data availability** The data that support the findings of this study are available from the corresponding author on request. The semi-empirical potential of iron developed in this work is public accessible [url to be updated].

**Contributions** K.M.H. and R.M.W. conceived the project. M.I.M. developed the semi-empirical potential and performed calculations. Y.S. performed simulations with persistent embryo method. Y.S. and F.Z. performed *ab initio* calculations on liquid and solid iron phases. Y.S. and M.I.M. wrote the manuscript. All authors discussed the results and contributed to paper writing.

**Competing interests** The authors declare no competing interests.

---

\* ys3339@columbia.edu

† mikhail.mendelev@gmail.com

- [1] Huguet, L., van Orman, J. A., Hauck, S. A. & Willard, M. A. Earth’s inner core nucleation paradox. *Earth Planet. Sci. Lett.* 487, 9–20 (2018).
- [2] Hirose, K., Labrosse, S. & Hernlund, J. Composition and State of the Core. *Annu. Rev. Earth Planet. Sci.* 41, 657–691 (2013).
- [3] Ross, M., Young, D. A. & Grover, R. Theory of the iron phase diagram at Earth core conditions. *J. Geophys. Res.* 95, 21713 (1990).
- [4] Matsui, M. & Anderson, O. L. The case for a body-centered cubic phase ( $\alpha'$ ) for iron at inner core conditions. *Phys. Earth Planet. Inter.* 103, 55–62 (1997).
- [5] Vočadlo, L. et al. Possible thermal and chemical stabilization of body-centered-cubic iron in the Earth’s core. *Nature* 424, 536–539 (2003).
- [6] Belonoshko, A. B. *et al.* Stabilization of body-centred cubic iron under inner-core conditions. *Nat. Geosci.* 10, 312–316 (2017).
- [7] Lister, J. R. & Buffett, B. A. The strength and efficiency of thermal and compositional convection in the geodynamo. *Phys. Earth Planet. Inter.* 91, 17–30 (1995).
- [8] Nimmo, F. Energetics of the Core. in *Treatise on Geophysics* vol. 8 pp. 27–55 (Elsevier, 2015).
- [9] Davies, C., Pozzo, M., Gubbins, D. & Alfè, D. Constraints from material properties on the dynamics and evolution of Earth’s core. *Nat. Geosci.* 8, 678–685 (2015).
- [10] Labrosse, S. Thermal evolution of the core with a high

- thermal conductivity. *Phys. Earth Planet. Inter.* 247, 36–55 (2015).
- [11] Badro, J., Siebert, J. & Nimmo, F. An early geodynamo driven by exsolution of mantle components from Earth’s core. *Nature* 536, 326–328 (2016).
  - [12] O’Rourke, J. G. & Stevenson, D. J. Powering Earth’s dynamo with magnesium precipitation from the core. *Nature* 529, 387–389 (2016).
  - [13] Hirose, K. *et al.* Crystallization of silicon dioxide and compositional evolution of the Earth’s core. *Nature* 543, 99–102 (2017).
  - [14] Kelton, K. F. & Greer, A. L. *Nucleation in condensed matter: application in materials and biology.* (Elsevier, 2010).
  - [15] Davies, C. J. Cooling history of Earth’s core with high thermal conductivity. *Phys. Earth Planet. Inter.* 247, 65–79 (2015).
  - [16] Davies, C. J., Pozzo, M. & Alfè, D. Assessing the inner core nucleation paradox with atomic-scale simulations. *Earth Planet. Sci. Lett.* 507, 1–9 (2019).
  - [17] De Yoreo, J. Crystal nucleation: more than one pathway. *Nat. Mater.* 12, 284–5 (2013).
  - [18] Ostwald, W. The formation and changes of solids. *Z. Phys. Chem* 22, 289–330 (1897).
  - [19] Herlach, D. M. Metastable materials solidified from undercooled melts. *J. Phys. Condens. Matter* 13, 7737–7751 (2001).
  - [20] Li, M., Lin, X., Song, G., Yang, G. & Zhou, Y. Microstructure evolution and metastable phase formation in undercooled Fe–30 at.% Co melt. *Mater. Sci. Eng. A* 268, 90–96 (1999).
  - [21] Notthoff, C., Feuerbacher, B., Franz, H., Herlach, D. M. & Holland-Moritz, D. Direct Determination of Metastable Phase Diagram by Synchrotron Radiation Experiments on Undercooled Metallic Melts. *Phys. Rev. Lett.* 86, 1038–1041 (2001).
  - [22] Shen, Y. C. & Oxtoby, D. W. bcc Symmetry in the Crystal-Melt Interface of Lennard-Jones Fluids Examined through Density Functional Theory. *Phys. Rev. Lett.* 77, 3585–3588 (1996).
  - [23] Song, H. & Mendelev, M. I. Molecular dynamics simulation of phase competition in terbium. *J. Chem. Phys.* 149, 244501 (2018).
  - [24] Zhou, J. *et al.* Observing crystal nucleation in four dimensions using atomic electron tomography. *Nature* 570, 500–503 (2019).
  - [25] Soso, G. C. *et al.* Crystal Nucleation in Liquids: Open Questions and Future Challenges in Molecular Dynamics Simulations. *Chem. Rev.* 116, 7078–7116 (2016).
  - [26] Mishin, Y., Asta, M. & Li, J. Atomistic modeling of interfaces and their impact on microstructure and properties. *Acta Mater.* 58, 1117–1151 (2010).
  - [27] Mendelev, M. I., Kramer, M. J., Becker, C. A. & Asta, M. Analysis of semi-empirical interatomic potentials appropriate for simulation of crystalline and liquid Al and Cu. *Philos. Mag.* 88, 1723–1750 (2008).
  - [28] Sun, Y. *et al.* Overcoming the Time Limitation in Molecular Dynamics Simulation of Crystal Nucleation: A Persistent-Embryo Approach. *Phys. Rev. Lett.* 120, 085703 (2018).
  - [29] Zhang, W.-J., Liu, Z.-Y., Liu, Z.-L. & Cai, L.-C. Melting curves and entropy of melting of iron under Earth’s core conditions. *Phys. Earth Planet. Inter.* 244, 69–77 (2015).
  - [30] Ackland, G. J., Mendelev, M. I., Srolovitz, D. J., Han, S. & Barashev, A. V. Development of an interatomic potential for phosphorus impurities in -iron. *J. Phys. Condens. Matter* 16, S2629–S2642 (2004).
  - [31] Belonoshko, A. B., Ahuja, R. & Johansson, B. Quasi-*Ab initio* Molecular Dynamic Study of Fe Melting. *Phys. Rev. Lett.* 84, 3638–3641 (2000).
  - [32] Laio, A., Bernard, S., Chiarotti, G. L., Scandolo, S. & Tosatti, E. Physics of iron at earth’s core conditions. *Science* 287, 1027–1030 (2000).
  - [33] Alfè, D., Price, G. D. & Gillan, M. J. Iron under Earth’s core conditions: Liquid-state thermodynamics and high-pressure melting curve from *ab initio* calculations. *Phys. Rev. B* 65, 165118 (2002).
  - [34] Sola, E. & Alfè, D. Melting of Iron under Earth’s Core Conditions from Diffusion Monte Carlo Free Energy Calculations. *Phys. Rev. Lett.* 103, 078501 (2009).
  - [35] Alfè, D. Temperature of the inner-core boundary of the Earth: Melting of iron at high pressure from first-principles coexistence simulations. *Phys. Rev. B* 79, 060101 (2009).
  - [36] Sun, T., Brodholt, J. P., Li, Y. & Vočadlo, L. Melting properties from *ab initio* free energy calculations: Iron at the Earth’s inner-core boundary. *Phys. Rev. B* 98, 224301 (2018).
  - [37] Anzellini, S., Dewaele, A., Mezouar, M., Loubeyre, P. & Morard, G. Melting of iron at earth’s inner core boundary based on fast X-ray diffraction. *Science* 340, 464–466 (2013).
  - [38] Li, J. *et al.* Shock Melting Curve of Iron: A Consensus on the Temperature at the Earth’s Inner Core Boundary. *Geophys. Res. Lett.* 47, e2020GL087758 (2020).
  - [39] Morris, J. R., Wang, C. Z., Ho, K. M. & Chan, C. T. Melting line of aluminum from simulations of coexisting phases. *Phys. Rev. B* 49, 3109–3115 (1994).
  - [40] Mendelev, M. I., Underwood, T. L. & Ackland, G. J. Development of an interatomic potential for the simulation of defects, plasticity, and phase transformations in titanium. *J. Chem. Phys.* 145, 154102 (2016).
  - [41] Sun, Y. *et al.* Temperature dependence of the solid-liquid interface free energy of Ni and Al from molecular dynamics simulation of nucleation. *J. Chem. Phys.* 149, 174501 (2018).
  - [42] Auer, S. & Frenkel, D. Numerical prediction of absolute crystallization rates in hard-sphere colloids. *J. Chem. Phys.* 120, 3015–29 (2004).
  - [43] Lin, J. F., Heinz, D. L., Campbell, A. J., Devine, J. M. & Shen, G. Iron-silicon alloy in earth’s core? *Science* 295, 313–315 (2002).
  - [44] Chen, B., Gao, L., Funakoshi, K. -i. & Li, J. Thermal expansion of iron-rich alloys and implications for the Earth’s core. *Proc. Natl. Acad. Sci.* 104, 9162–9167 (2007).
  - [45] Dubrovinsky, L. *et al.* Body-centered cubic iron-nickel alloy in earth’s core. *Science* 316, 1880–1883 (2007).
  - [46] Kádas, K., Vitos, L., Johansson, B. & Ahuja, R. Stability of body-centered cubic iron–magnesium alloys in the Earth’s inner core. *Proc. Natl. Acad. Sci.* 106, 15560–15562 (2009).
  - [47] Wang, R. *et al.* Prediction of crystal structures and motifs in the Fe-Mg-O system at Earth’s core pressures. *arXiv* 2102.03402 (2021).
  - [48] Belonoshko, A. B., Skorodumova, N. V., Rosengren, A. & Johansson, B. Elastic Anisotropy of Earth’s Inner Core. *Science* 319, 797–800 (2008).

- [49] Wang, T., Song, X. & Xia, H. H. Equatorial anisotropy in the inner part of Earth's inner core from autocorrelation of earthquake coda. *Nat. Geosci.* 8, 224–227 (2015).
- [50] Stephenson, J., Tkalčić, H. & Sambridge, M. Evidence for the Innermost Inner Core: Robust Parameter Search for Radially Varying Anisotropy Using the Neighborhood Algorithm. *J. Geophys. Res. Solid Earth* 126, e2020JB020545 (2021).
- [51] Kresse, G. & Furthmüller, J. Efficient iterative schemes for *ab initio* total-energy calculations using a plane-wave basis set. *Phys. Rev. B* 54, 11169–11186 (1996).
- [52] Mermin, N. D. Thermal properties of the inhomogeneous electron gas. *Phys. Rev.* 137, A1441 (1965).
- [53] Wentzcovitch, R. M., Martins, J. L. & Allen, P. B. Energy versus free-energy conservation in first-principles molecular dynamics. *Phys. Rev. B* 45, 11372–11374 (1992).
- [54] Nosé, S. A unified formulation of the constant temperature molecular dynamics methods. *J. Chem. Phys.* 81, 511 (1984).
- [55] Brown, W. M., Wang, P., Plimpton, S. J. & Tharrington, A. N. Implementing molecular dynamics on hybrid high performance computers—short range forces. *Comput. Phys. Commun.* 182, 898–911 (2011).
- [56] Brown, W. M., Kohlmeyer, A., Plimpton, S. J. & Tharrington, A. N. Implementing molecular dynamics on hybrid high performance computers – Particle–particle particle–mesh. *Comput. Phys. Commun.* 183, 449–459 (2012).
- [57] Brown, W. M. & Yamada, M. Implementing molecular dynamics on hybrid high performance computers - Three-body potentials. *Comput. Phys. Commun.* 184, 2785–2793 (2013).
- [58] Daw, M. S. & Baskes, M. I. Embedded-atom method: Derivation and application to impurities, surfaces, and other defects in metals. *Phys. Rev. B* 29, 6443–6453 (1984).



### Two-step nucleation of the Earth's inner core

Yang Sun<sup>1</sup>, Feng Zhang<sup>2</sup>, Mikhail I. Mendelev<sup>2</sup>, Renata M. Wentzcovitch<sup>1,3,4</sup>, Kai-Ming Ho<sup>5</sup>

<sup>1</sup>Department of Applied Physics and Applied Mathematics, Columbia University, New York, NY 10027, USA

<sup>2</sup>Ames Laboratory, US Department of Energy, Ames, IA 50011, USA

<sup>3</sup>Department of Earth and Environmental Sciences, Columbia University, New York, NY 10027, USA

<sup>4</sup>Lamont–Doherty Earth Observatory, Columbia University, Palisades, NY 10964, USA

<sup>5</sup>Department of Physics, Iowa State University, Ames, IA 50011, USA

Correspondence to [ys3339@columbia.edu](mailto:ys3339@columbia.edu) (Y.S.) or [mikhail.mendelev@gmail.com](mailto:mikhail.mendelev@gmail.com) (M.I.M.)

This supplementary information contains details of semi-empirical potential development in Note S1, the calculation of the kinetic prefactor in Note S2, the effect of input parameters on the hcp waiting time in Note S3, and classification of hcp, bcc, and liquid with order parameters in Note S4.

### Supplementary Note 1 | Development of semi-empirical potential

Several groups of target properties were used in the development of the embedded atom method (EAM) potential for iron. The first group consisted of basic bcc Fe properties at  $T=0$  and  $p=0$  listed in Table S1. This is a standard set routinely used in development procedures for semi-empirical potentials. Since the condition of  $T=0$  and  $p=0$  is very far from the conditions we were interested in, these properties were fitted with low weights. The examination of Table S1 shows that the developed potential reproduces these properties reasonably well (obviously, the semi-empirical potentials explicitly fitted to these conditions provide much better reproduction of these properties).

**Table S1 | Fe bcc properties at  $T=0$  and  $p=0$ .**

Property	Target value	EAM potential
Lattice parameter ( $\text{\AA}$ )	2.855	2.844
Cohesive energy (eV/atom)	-4.316	-4.022
Unrelaxed vacancy formation energy (eV/atom)	1.84	1.53
$C_{11}$ (GPa)	243	246
$C_{12}$ (GPa)	145	141
$C_{44}$ (GPa)	116	103

Next, we approximately extracted from the *ab initio* molecular dynamics (AIMD) simulation the hcp lattice parameters at two endpoints of the temperature-pressure range we were interested in ( $T=4000$  K/ $p=140$  GPa and  $T=6000$  K/ $p=350$  GPa). This was done by manually adjusting the hcp lattice parameters at these conditions. The accuracy of such a procedure was not very high such that the difference between  $\sigma_{xx}$  and  $\sigma_{zz}$  could be as significant as 14 GPa. Fortunately, that was not the problem with our fitting procedure. In reality, the potential was fitted not to the lattice parameters but to the stresses corresponding to the given lattice parameters. These stresses were determined from the AIMD simulation with sufficient accuracy. We will come back to this point below. After a few iterations of the potential development procedure, we used the current potential to determine the lattice parameters at  $T=5500$  K/ $p=212$  GPa. We ran AIMD to determine the stresses corresponding to these lattice parameters. In this case, the difference between  $\sigma_{xx}$  and  $\sigma_{zz}$  were less than 1 GPa. The new data were added to the list of target properties in the potential development procedure. We also included the same type of AIMD data for the bcc phase at  $T=6000$  K/ $p=350$  GPa (in this case, there is just one lattice parameter to fit).

**Table S2 | The elastic response tensors between AIMD and MD with EAM potential.**

Conditions	Tensor components (GPa)	AIMD	EAM
hcp at T=4000 K p=140 GPa	$R_{11}$	820	758
	$R_{12}$	589	614
	$R_{13}$	389	467
	$R_{33}$	832	810
	$R_{44}$	122	105
hcp at T=5500 K p=212 GPa	$R_{11}$	1064	1015
	$R_{12}$	784	860
	$R_{13}$	671	740
	$R_{33}$	1185	1229
	$R_{44}$	122	131
hcp at T=6000 K p=350 GPa	$R_{11}$	1646	1548
	$R_{12}$	1235	1286
	$R_{13}$	1009	1142
	$R_{33}$	1758	1834
	$R_{44}$	216	203
bcc at T=6000 K p=350 GPa	$R_{11}$	1318	1291
	$R_{12}$	1236	1229
	$R_{44}$	287	307

Three types of deformation were applied to each of the hcp models to get non-zero  $\varepsilon_{xx}$ ,  $\varepsilon_{zz}$ , and  $\varepsilon_{yz}$  (the absolute values of  $\varepsilon_{\alpha\beta}$  were 0.01). The stress tensor components were determined from the AIMD simulation for each case. The differences between these stress tensor components and the components of the stress tensors of the corresponding initial models divided by the deformation value were defined as the elastic responses,  $R_{ij}$ .  $R_{ij}$  would be the same as the corresponding elastic constants if all components of the stress tensor of the initial model were zero.  $R_{ij}$  constants reflect the crystal response to the applied deformation. A good fitting to these constants should warrant the reproduction of the correct elastic properties of the considered phases. The obtained AIMD values are presented in Table S2. It is important to emphasize that the bcc phase did not transform

to any other lattice under applied deformation during the AIMD simulation, demonstrating that this phase is at least metastable (not unstable) at these conditions. The examination of Table S2 shows that the developed potential reasonably well reproduces the elastic responses obtained from the AIMD simulation.

Since we were interested in simulating nucleation from the liquid phase, it is essential to include the liquid density and structure data obtained from the AIMD simulation in the potential development procedure. The method to achieve this was described in <sup>1</sup>. Figure S1 shows the pair correlation functions of liquid Fe obtained from the AIMD simulation and classical MD (CMD) simulation at Earth's core conditions utilizing the developed EAM potential. Examination of this figure indicates that the developed potential provides a pretty reasonable agreement with the AIMD data.

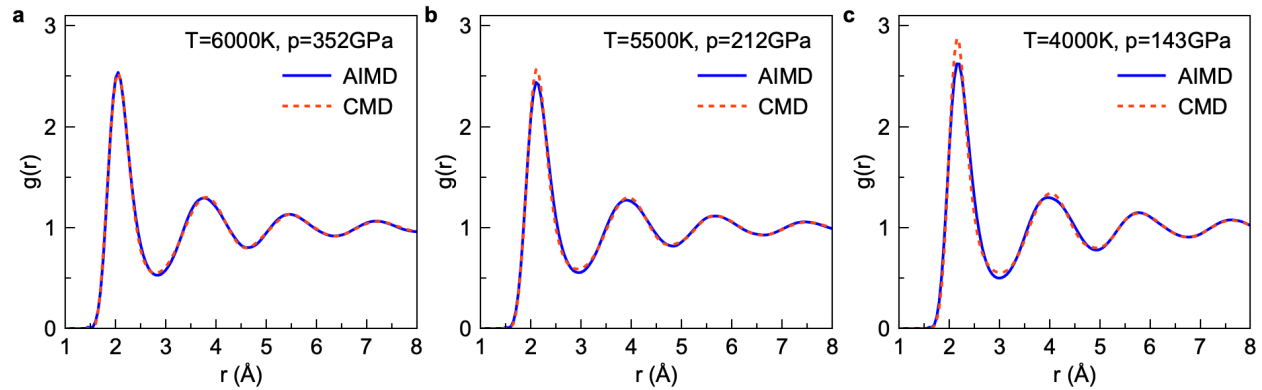


**Figure S1 | Pair correlation functions of liquid Fe under the Earth's core conditions between AIMD and CMD with the present potential. a, T=6000K and p=352GPa. b, T=5500K and p=212 GPa. c, T=4000K and p=143 GPa.**

To test the ability of the developed potential on the predictions of the solidification under the Earth's core conditions, we performed the following test. First, we choose two temperatures for testing: T=4800 K and T=5800 K. Using the developed EAM potential, we created hcp, bcc, and liquid models at these temperatures and p=323 GPa. Then we performed the AIMD NVT simulations using these models, which led to different stresses and pressures, as shown in Table S3. The largest deviations were obtained for the hcp phase at T=4800 K. Such deviations in pressure correspond to about 0.7% for the deviation in the atomic density.

Next, two types of deformation were applied to hcp models to get non-zero  $\epsilon_{xx}$  and  $\epsilon_{zz}$ . Only one type of deformation was applied to the bcc models for a non-zero value of  $\epsilon_{xx}$ . The

absolute values of  $\varepsilon_{\alpha\beta}$  were 0.01. Entire stress tensors were determined from the AIMD simulation for each case. These data allowed us to determine the lattice parameters at the same pressure as was obtained from AIMD simulations for liquid models. New AIMD simulations were performed with these lattice parameters to confirm that all diagonal components of the stress tensors are the same as the liquid pressure and to get the phase energies, allowing us to obtain the latent heats provided in Table S3. The examination of the data presented in Table S3 shows that the developed potential slightly overestimates the c/a ratio for the hcp phase. However, the key property for the simulation of the crystallization is the latent heat and the examination of the data presented in Table S3 shows that the developed potential provides an excellent agreement with the AIMD data.

**Table S3 | Comparison between developed EAM potential and AIMD.**

Property	AIMD	EAM
P (liquid at $\rho=0.1437$ atom/ $\text{\AA}^3$ and $T=4800$ K) (GPa)	322.6	323.0
P (liquid at $\rho=0.1429$ atom/ $\text{\AA}^3$ and $T=5800$ K) (GPa)	326.9	323.0
$\sigma_{xx}$ (hcp at $\rho=0.1450$ atom/ $\text{\AA}^3$ and $T=4800$ K) (GPa)	315.8	323.0
$\sigma_{zz}$ (hcp at $\rho=0.1450$ atom/ $\text{\AA}^3$ and $T=4800$ K) (GPa) <sup>§</sup>	311.8	323.0
$\sigma_{xx}$ (hcp at $\rho=0.1443$ atom/ $\text{\AA}^3$ and $T=5800$ K) (GPa)	321.8	323.0
$\sigma_{zz}$ (hcp at $\rho=0.1443$ atom/ $\text{\AA}^3$ and $T=5800$ K) (GPa) <sup>§</sup>	319.8	323.0
p (bcc at $\rho=0.1451$ atom/ $\text{\AA}^3$ and $T=4800$ K) (GPa)	323.9	323.0
p (bcc at $\rho=0.1443$ atom/ $\text{\AA}^3$ and $T=5800$ K) (GPa)	328.7	323.0
c/a (hcp at $T=4800$ K and $p\approx 323$ GPa)	1.622	1.629
c/a (hcp at $T=5800$ K and $p\approx 323$ GPa)	1.624	1.628
$\Delta H_m$ (eV/atom) (hcp at $T=4800$ K and $p=323$ GPa)	0.529	0.521
$\Delta H_m$ (eV/atom) (hcp at $T=5800$ K and $p=323$ GPa)	0.540	0.524
$\Delta H_m$ (eV/atom) (bcc at $T=4800$ K and $p=323$ GPa)	0.365	0.367
$\Delta H_m$ (eV/atom) (bcc at $T=5800$ K and $p=323$ GPa)	0.394	0.394

Finally, we determined the melting temperatures for the hcp and bcc phases at several pressures using the coexistence approach proposed in Ref. <sup>2</sup>. The results are shown in Fig. 1 of the

<sup>§</sup> In the case of the hcp phase the lattice parameters were chosen using the EAM potential which provided  $\sigma_{xx}=\sigma_{zz}$ ; since the AIMD leads to a different c/a ratio,  $\sigma_{xx}\neq\sigma_{zz}$  for the same lattice parameters.

main text. Overall, our current melting curve provides the closest agreement to the recent high-pressure experiments for the hcp phases compared to other previous calculated results. Moreover, the developed EAM potential provides the hcp phase as the ground state under the Earth's inner core. It also predicts that the bcc melting temperature is close to the hcp melting temperature at 360 GPa.

Since this potential provides a good melting curve of the hcp phase compared to literature data, a good agreement of elastic constants compared to the AIMD data, and especially excellent agreement for the latent heats, it is suitable for crystallization simulation under the Earth's core conditions.

### Supplementary Note 2 | Kinetic prefactor $\kappa$ in nucleation rate

From Classical nucleation theory, the nucleation rate,  $J$ , can be calculated as  $J = \kappa \exp(-\Delta G^*/k_B T)$ , where  $\Delta G^*$  is the nucleation barrier,  $k_B$  is the Boltzmann constant, and  $\kappa$  is a kinetic prefactor. The kinetic prefactor  $\kappa$  can be derived from the steady-state model<sup>3</sup> as

$$\kappa = \rho_L f^+ \sqrt{\frac{|\Delta\mu|}{6\pi k_B T N^*}}, \quad (\text{S1})$$

where  $f^+$  is the attachment rate of a single atom to the critical nucleus and  $\rho_L$  is the liquid density,  $\Delta\mu$  is the chemical potential difference between bulk solid and liquid,  $N^*$  is the critical nucleus size. As demonstrated by Auer and Frenkel<sup>4</sup>, the attachment rate can be computed as the effective diffusion constant for the size change of the critical nucleus as  $f^+ = \frac{\langle |\Delta N^*(t)|^2 \rangle}{2t}$ . Therefore, we employed the iso-configurational ensemble<sup>5</sup> simulation to measure  $f^+$  using the critical nucleus obtained from the PEM-MD simulations. In Fig. S2a, 60 independent MD runs starting from the same atomic configuration but with atomic momenta randomly assigned using the Maxwell distribution are shown. The critical nucleus melted in half of the MD runs and grew in the other half runs, which validates the determination of the critical nucleus size. The measured  $f^+$  of both hcp and bcc are shown in Fig. S2b. The temperature dependence of obtained  $f^+$  can be well fit to the classical kinetic model of atom attachment<sup>3</sup> as

$$f^+ = s N^{*2/3} \frac{6D}{\lambda^2}, \quad (\text{S2})$$

where  $D$  is the liquid diffusivity measured from MD simulation. The hcp nucleus shows a systematically higher attachment rate than that of the bcc nucleus. It should be noted that the effect

of  $f^+$  on the nucleation rate is much smaller than the  $\Delta G^*$  as  $J$  depends exponentially on  $\Delta G^*$  in Eq. (S1).

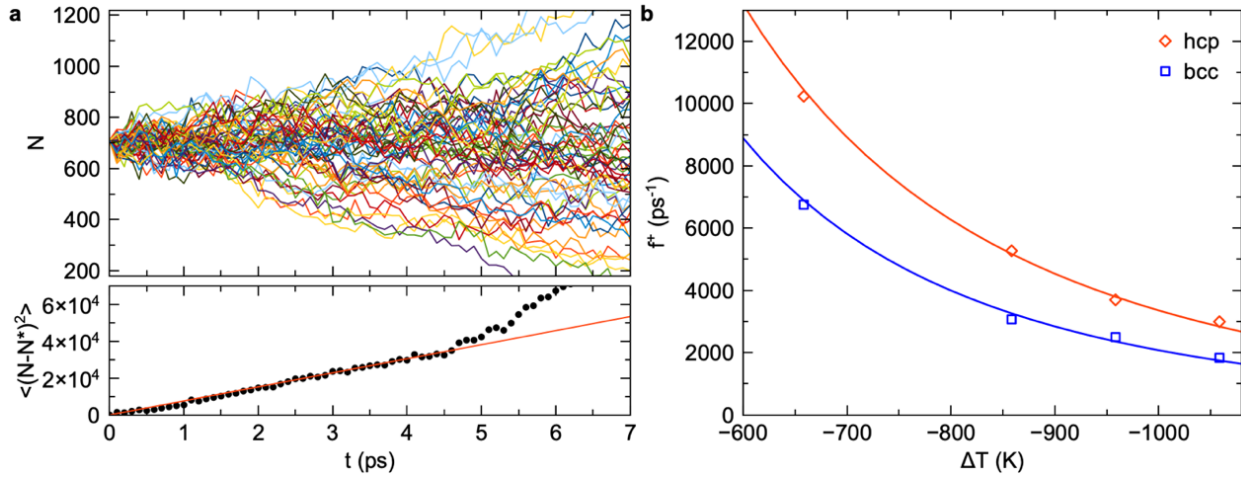


**Figure S2 | Measurement of the attachment rate for the hcp and bcc phases.** **a**, Iso-configurational ensemble of the hcp critical nucleus obtained at 323 GPa and  $\Delta T = -958$  K. 60 MD runs are performed starting from the same configuration but with different initial atomic velocities. The bottom panel shows the ensemble average of the nucleus change  $\langle |\Delta N^*(t)|^2 \rangle = \langle (N(t) - N^*)^2 \rangle$ . The red line indicates the linear fitting to the first 4 ps used to obtain the attachment rate. **b**, The attachment rate as a function of undercooling temperature for the hcp and bcc phases. The symbols are data points obtained from the iso-configurational ensemble averaging. The solid line is fitting to Eqn. (S2)

### Supplementary Note 3 | Effect of input parameters on the waiting time

To elucidate the effect of the input parameters on the nucleation waiting time of the hcp phase, we substituted the input parameters obtained from the present study with those from Ref. <sup>6</sup>. Figure S3a shows the comparison of the waiting time. It indicates that the different  $\Delta\mu$  is the major factor that causes the difference between the current data and the one in <sup>6</sup>. Figure S3b shows the comparison of  $\Delta\mu$  obtained in these two works. Using the melting temperature from <sup>6</sup> leads to a decreased  $\Delta\mu$ . The original  $\Delta\mu$  from <sup>6</sup> is even smaller. Because  $\Delta\mu$  is essentially correlated with the latent heat based on the Gibbs-Helmholtz equations, these comparisons elucidate the strong effect of the latent heat on the final results. Note that the latent heat provided by the potential developed in the present study is in excellent agreement with the AIMD data as shown in Fig. 1 in the main text.

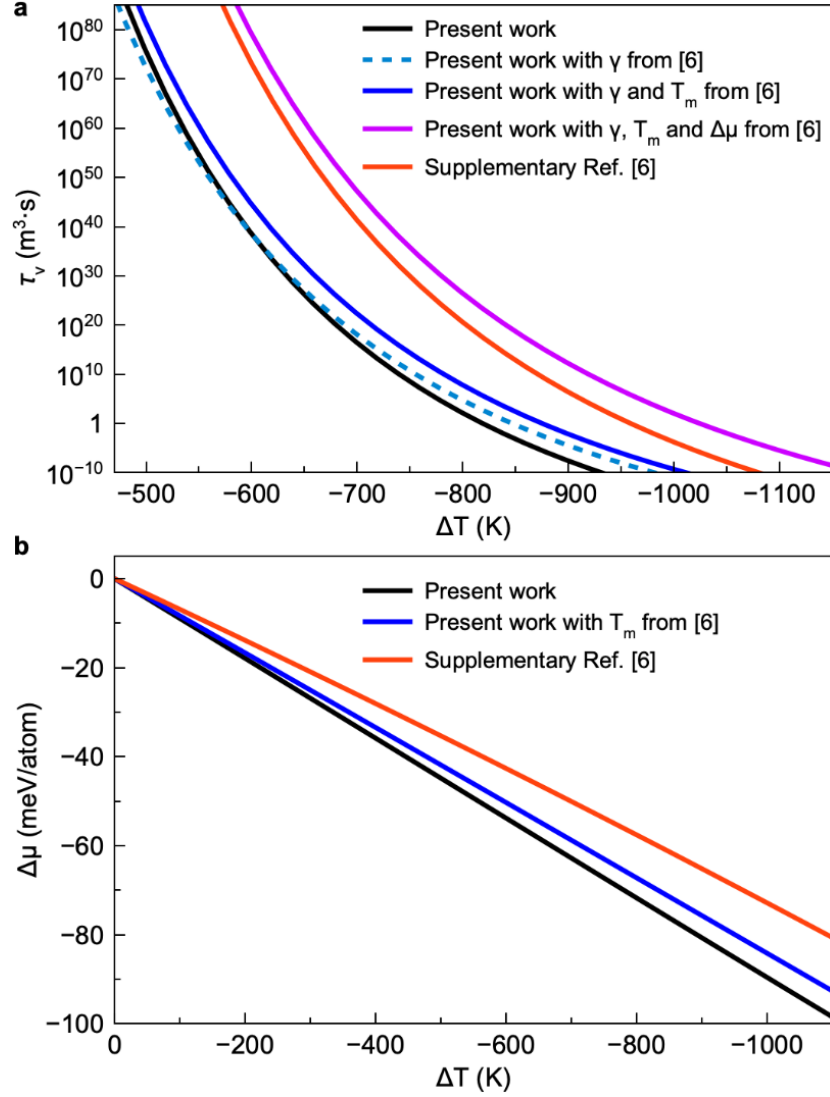


**Figure S3** | The waiting time and the chemical potential difference for the hcp phase nucleation calculated in the present study and substitution of the current input parameters by those from <sup>6</sup>.

#### Supplementary Note 4 | Order parameters

To identify the nucleus type and size in this study, we employ two structural order parameters, bond-orientational order (BOO) parameter <sup>7</sup> and cluster alignment (CA) method <sup>8</sup>. The BOO parameter is based on the correlation between the structures of any two neighbor atoms  $i$  and  $j$  as  $S_{ij} = \sum_{m=-6}^6 q_{6m}(i) \cdot q_{6m}^*(j)$ , where  $q_{6m}(i) = \frac{1}{N_b(i)} \sum_{j=1}^{N_b(i)} Y_{lm}(\vec{r}_{ij})$  is the Steinhardt parameter,  $Y_{lm}(\vec{r}_{ij})$  are the spherical harmonics,  $N_b(i)$  is the number of nearest neighbors of atom  $i$  and  $\vec{r}_{ij}$  is the vector connecting it with its neighbor  $j$ . Two neighboring atoms  $i$  and  $j$  are considered to be connected when  $S_{ij}$  exceeds a threshold  $S_c$ . To choose a reasonable value of  $S_c$ , an "equal



mislabeling" method <sup>9</sup> was used so that the probability of mislabeling atoms in the bulk liquid as solid-like atoms is the same as the probability of mislabeling atoms in bulk solid as liquid-like atoms. This approach works well when one needs to detect bulk solid atoms within a bulk liquid. However, it tends to mislabel solid atoms at the solid-liquid interface. Therefore it requires another threshold  $\xi$  to account for the number of solid-like neighbors. Here the threshold value,  $\xi_c$ , is chosen to be 6 for the hcp-liquid interfaces and 7 for the bcc-liquid interface. BOO parameter is computed on the fly of PEM-MD to identify the solid-like atoms during the simulation efficiently.

As being demonstrated in <sup>10,11</sup>, the nucleus size can be somewhat sensitive to the choice of order parameters. Therefore, in addition to the BOO, CA method <sup>8</sup> was employed to validate the nucleus size by post-processing the simulation trajectory of PEM. The CA method differentiates complex crystal structures by computing the minimal root-mean-square deviation (RMSD) between the atomic cluster and the perfect crystal motifs <sup>12,13</sup>. In Fig. S4, we show the RMSD distributions of atoms in liquid, hcp, and bcc phases under the core conditions. It indicates a good performance of CA on distinguishing the hcp, bcc, and liquid for the present system.

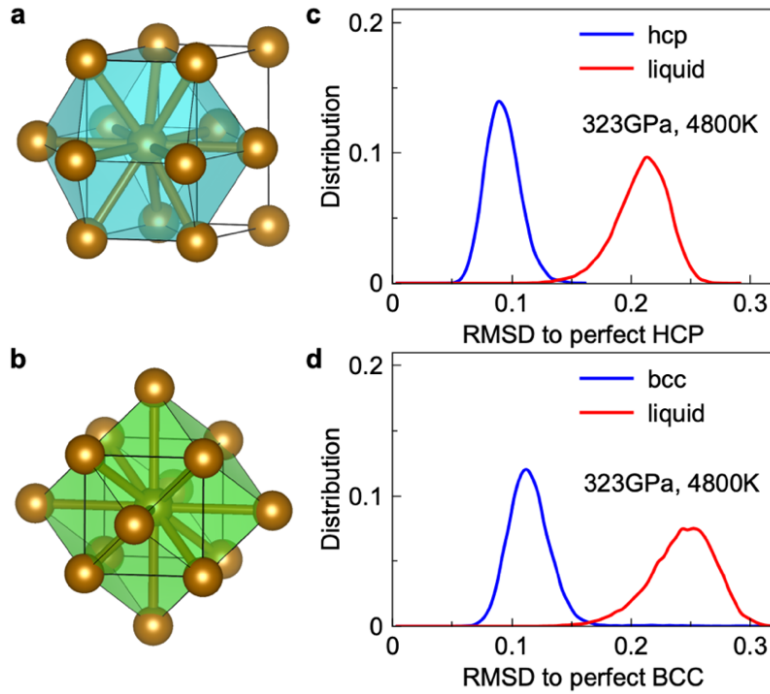


**Figure S4 | Cluster alignment to differentiate the HCP and BCC phases from the liquid.** **a** and **b** show the hcp and bcc lattices and the clusters (colored polyhedral) used as hcp and bcc templates, respectively. **c** and **d** show the different distribution of root-mean-square deviation (RMSD) of hcp, bcc and liquid.

## Supplementary References

1. Mendeleev, M. I. & Srolovitz, D. J. Determination of alloy interatomic potentials from liquid-state diffraction data. *Phys. Rev. B* **66**, 014205 (2002).
2. Morris, J. R., Wang, C. Z., Ho, K. M. & Chan, C. T. Melting line of aluminum from simulations of coexisting phases. *Phys. Rev. B* **49**, 3109–3115 (1994).
3. Kelton, K. F. & Greer, A. L. *Nucleation in condensed matter: application in materials and biology*. (Elsevier, 2010).
4. Auer, S. & Frenkel, D. Numerical prediction of absolute crystallization rates in hard-sphere colloids. *J. Chem. Phys.* **120**, 3015–29 (2004).
5. Widmer-Cooper, A., Harrowell, P. & Fynewever, H. How reproducible are dynamic heterogeneities in a supercooled liquid? *Phys. Rev. Lett.* **93**, 135701 (2004).
6. Davies, C. J., Pozzo, M. & Alfè, D. Assessing the inner core nucleation paradox with atomic-scale simulations. *Earth Planet. Sci. Lett.* **507**, 1–9 (2019).
7. Steinhardt, P. J., Nelson, D. R. & Ronchetti, M. Bond-orientational order in liquids and glasses. *Phys. Rev. B* **28**, 784–805 (1983).
8. Fang, X. W., Wang, C. Z., Yao, Y. X., Ding, Z. J. & Ho, K. M. Atomistic cluster alignment method for local order mining in liquids and glasses. *Phys. Rev. B* **82**, 184204 (2010).
9. Espinosa, J. R., Vega, C., Valeriani, C. & Sanz, E. Seeding approach to crystal nucleation. *J. Chem. Phys.* **144**, 034501 (2016).
10. Zimmermann, N. E. R. *et al.* NaCl nucleation from brine in seeded simulations: Sources of uncertainty in rate estimates. *J. Chem. Phys.* **148**, 222838 (2018).
11. Sun, Y. *et al.* Temperature dependence of the solid-liquid interface free energy of Ni and Al from molecular dynamics simulation of nucleation. *J. Chem. Phys.* **149**, 174501 (2018).
12. Sun, Y. *et al.* ‘Crystal Genes’ in Metallic Liquids and Glasses. *Sci. Rep.* **6**, 23734 (2016).
13. Ren, S. *et al.* Phase Diagram and Structure Map of Binary Nanoparticle Superlattices from a Lennard-Jones Model. *ACS Nano* **14**, 6795–6802 (2020).